Title

Optical properties of biomimetic probes engineered from erythrocytes

Journal

Nanotechnology, 28(3)

ISSN

0957-4484

Authors

Burns, Joshua M
Saager, Rolf
Majaron, Boris
et al.

Publication Date

2017-01-20

DOI

10.1088/1361-6528/28/3/035101

Peer reviewed

Published in final edited form as:

Nanotechnology. 2017 January 20; 28(3): 035101. doi:10.1088/1361-6528/28/3/035101.

Optical properties of biomimetic probes engineered from erythrocytes

Joshua M. Burns[1], **Rolf Saager**[2], **Boris Majaron**[3], **Wangcun Jia**[2], and **Bahman Anvari**[1,2]

[1]Department of Bioengineering, University of California, Riverside, Riverside, CA 92521, USA

[2]Beckman Laser Institute and Medical Clinic, University of California, Irvine, Irvine, CA 92612, USA

[3]Department of Complex Matter, Jožef Stefan Institute, Jamova 39, SI-1000 Ljubljana, Slovenia

Abstract

Light-activated theranostic materials offer a potential platform for optical imaging and phototherapeutic applications. We have engineered constructs derived from erythrocytes, which can be doped with the FDA-approved near infrared (NIR) chromophore, indocyanine green (ICG). We refer to these constructs as NIR erythrocyte-mimicking transducers (NETs). Herein, we investigated the effects of changing the NETs mean diameter from micron- (≈ 4 μm) to nano- (≈ 90 nm) scale, and the ICG concentration utilized in the fabrication of NETs from 5 to 20 μM on the resulting absorption and scattering characteristics of the NETs. Our approach consisted of integrating sphere-based measurements of light transmittance and reflectance, and subsequent utilization of these measurements in an inverse adding-doubling algorithm to estimate the absorption (μ_a) and reduced scattering (μ_s') coefficients of these NETs. For a given NETs diameter, values of μ_a increased over the approximate spectral band of 630 – 860 nm with increasing ICG concentration. Micron-sized NETs produced the highest peak value of μ_a when using ICG concentrations of 10 and 20 μM, and showed increased values of μ_s' as compared to nano-sized NETs. Spectral profiles of μ_s' for these NETs showed a trend consistent with Mie scattering behavior for spherical objects. For all NETs investigated, changing the ICG concentration minimally affected the scattering characteristics. A Monte Carlo-based model of light distribution showed that the presence of these NETs enhanced the fluence levels within simulated blood vessels. These results provide important data towards determining the appropriate light dosimetry parameters for an intended light-based biomedical application of NETs.

Keywords

light; imaging; nanomaterials; nanoparticles; phototherapy; red blood cells; theranostics

1. Introduction

Light-activated theranostic materials present a platform for potential clinical optical imaging and phototherapeutic applications [1–6]. Materials that are activated by near infrared (NIR) excitation wavelengths (λ) are especially advantageous since relatively deep (on the order of ≈ 3–5 cm) optical imaging and phototherapy can be achieved over this spectral band. To-date, indocyanine green (ICG) remains the only NIR chromophore approved by United Sates

Food and Drug Administration (FDA) for specific clinical applications including ophthalmic angiography, cardiocirculatory measurements, assessment of hepatic function, and blood flow evaluation [7–9]. ICG has also been investigated for potential applications ranging from sentinel lymph node mapping in patients with different types of cancer to imaging intracranial aneurysm and cerebral arteriovenous malformations [10–17]. Additionally, ICG has been investigated as a photosensitizer for photodynamic therapy (PDT) of choroidal melanomas, and as a photothermal agent for treatment of port wine stains (PWSs) [18–20].

Despite its wide utility in clinical medicine, ICG's major drawbacks are its non-specificity and short lifetime within circulation (half-life on the order of 2–4 minutes). Encapsulation of ICG within various constructs, including micelles, liposomes, silica, and synthetic polymers has been investigated as an approach to increase circulation time of ICG and reduce its non-specific interactions [21–31].

More recently, mammalian cells such as erythrocytes, lymphocytes, and macrophages, or constructs derived from them, are receiving increased attention as new types of platforms for the delivery of therapeutic or imaging agents [32–37]. Use of erythrocytes is particularly attractive due to their naturally long circulation time (≈ 90–120 days), attributed to the presence of "self-marker" membrane proteins [38,39]. Hemoglobin-depleted red blood cells, erythrocyte ghosts (EGs), have been doped with iron oxide and gold nanoparticles to enhance contrast in magnetic resonance imaging (MRI) and dynamic X-ray imaging of blood flow [40–43]. ICG-loaded EGs have been used to characterize the movement of erythrocytes in choriocapillaries and retinal capillaries of rabbits and monkeys [44]. In addition to imaging, erythrocytes have been doped with fluorescein isothiocyanate to create biosensors for monitoring changes in plasma analytes and extracellular pH [45,46].

We recently reported the first demonstration of successful engineering of nano-sized vesicles derived from erythrocytes loaded with ICG for fluorescence imaging and photothermal destruction of human cells [47]. We refer to these constructs as NIR erythrocyte-mimicking transducers (NETs). A key advantage of erythrocyte-derived constructs as compared to liposomal particles is that the former can potentially have extended circulation time due to preserved membrane proteins that prevent phagocytosis by immune cells. In a previous study [48], we demonstrated that CD47, a membrane glycoprotein, which impedes phagocytosis [38,39], remains on the surface of NETs. Other investigators have reported that polymeric nano-constructs, coated with erythrocyte-derived membranes, were retained in mice blood for three days with circulation half-life of nearly 40 hours [49].

A particular feature of NETs is that their diameter (d_{NETs}) can be tuned to various sizes by appropriate mechanical manipulation procedures, and their ICG content can be changed during the fabrication process. These parameters are important in that d_{NETs} can influence the NETs biodistribution dynamics, and in combination with the ICG content, they will determine the optical properties of NETs. Such properties are ultimately important in selection of the appropriate light dosimetry parameters for an intended light-based biomedical application, as well as the development of mathematical models to predict the optical response of biological tissues containing NETs.

Herein, we present the first report on the optical properties of NETs as a function of their diameters, and ICG concentration utilized in fabricating them. Specifically, we examine micron- and nano-sized NETs formed without and with mechanical extrusion methods, respectively. The nano-sized NETs have relevance to cancer imaging and phototherapy. Specifically, the enhanced permeability and retention (EPR) effect of tumors, induced by leaky tumor vasculature and impaired lymphatic drainage, may provide the basis for the delivery of NETs into tumors [50–52]. The effects of changes in NETs diameter from micron to nano scale are relevant to imaging and photothermal destruction capability of vascular abnormalities such as those found in port wine stain lesions in skin, and subsequent selection of optimal imaging and irradiation parameters in this dermatological application. Finally, using a Monte Carlo simulation approach, we demonstrate the effects of NETs diameter and ICG concentration on the resulting light distribution within a simulated blood vessel, a biologically relevant target of light in various clinical applications.

2. Methods and Materials

2.1. Fabrication of NETs

Whole bovine blood was centrifuged at 1,300 relative centrifugal force (rcf) for five minutes at 4 °C to separate the erythrocytes from the plasma and buffy coat. Isolated erythrocytes were then washed in 1 ml of cold 1x phosphate buffered saline (PBS) (310 mOsm, pH 8), and centrifuged at 1,300 rcf for five minutes at 4 °C. Packed erythrocytes were transferred to an ultracentrifuge tube and suspended in 50 ml of hypotonic buffer (0.5x PBS, 155 mOsm, pH 8) and incubated at 4 °C for 30 minutes. Further hemoglobin depletion was not performed because of the possible deleterious effects on erythrocyte shape with more aggressive hypotonic treatments.

Erythrocyte ghosts (EGs), formed by hypotonic treatment of red blood cells (RBCs), were re-suspended in 1x PBS, and separated into three sample sets. EGs in Set I were extruded 40 times through 400 nm polycarbonate porous membranes (Nuclepore Track-Etched Membranes, Whatman, Florham Park, New York) (single extrusion method). EGs in Set II were extruded through 40 times 400 nm polycarbonate membranes, followed by 40 more extrusions through 100 nm polycarbonate membranes (double extrusion method). EGs in set III were not extruded. Extrusion of EGs in sets I and II resulted in formation of spherical nano-sized particles through cleavage and reformation of the membrane [53,54], whereas EGs in set III remained micron-sized. The filters used for extrusion are cylindrical with nano-sized diameters, forming narrow and long tubes (tube length > tube diameter). Similar to lipid vesicles, when spherical erythrocyte ghosts (or red blood cells) are extruded through these filters, they likely acquire cylindrical shapes and break into smaller structures when they reach the end of the filters, and re-assemble into nano-sized vesicles [53]. The bilayer of the erythrocyte ghost ruptures when the induced membrane tension due to applied pressure exceeds the lysis tension [54].

To ensure that nearly the same amount of erythrocytes-derived membranes were present among the samples in all three sets, extruded samples (sets I and II) were diluted appropriately so that the absorbance value at 280 nm (associated with membrane proteins) in these samples matched the value for non-extruded samples (set III). Therefore, with the

same amount of membrane available, we expect that there would be a smaller number of micron-sized NETs than nano-sized NETs.

EGs in all sets were separated into aliquots, and incubated with 3 ml of hypotonic buffer (Na_2HPO_4/ $Na_2H_2PO_4$, 140 mOsm, pH 5.8). To this solution, we added 3 ml of ICG dissolved in water at different concentrations so that the final concentrations of ICG in the loading solvent were 0, 5, 10, and 20 μM. Suspensions were then incubated for five minutes at 4 °C in dark, centrifuged at 25,000 rcf for 20 minutes, and washed twice in 1x PBS to remove any non-encapsulated ICG. ICG-loaded EGs (NETs) were re-suspended in cold 1x PBS buffer solution. Prior to characterization of optical properties, NETs samples were centrifuged and supernatant removed.

2.2. Characterization of NETs

Phase contrast images of un-extruded NETs (set III) were obtained using a microscope (Nikon Ti-Eclipse, Melville, New York), and an electron multiplier gained CCD camera (Quant EM- CCD, Hamamatsu, Japan) at integration time of 0.1 s and gain of 1.0. We estimated the diameter of un-extruded NETs using ImageJ software, and determined the mean and standard deviation (SD) of the population sample. The hydrodynamic diameters of nano-sized NETs (sets I and II) suspended in 1x PBS were measured by dynamic light scattering (DLS) (Zetasizer NanoZS90, Malvern Instruments Ltd, Malvern, United Kingdom).

We used an integrating sphere (4P-GPS-033-SL, Labsphere, North Sutton, New Hampshire) to measure the percent transmittance (T) and reflectance (R) from the samples (figure 1). Visible-NIR (from 400 – 1000 nm) light from a broadband source (HL2000 20W Quartz-Tungsten-Halogen lamp, Ocean Optics, Dunedin, Florida) was collimated, and an aperture mask used to create a 4 mm diameter beam. A 400 micron fiber collected the transmitted or reflected light at the detector port, placed at 90° from the entrance or exit ports, respectively, and delivered it to a spectrometer (Prime-X, B&W Tek, Newark, Delaware).

Measurements of T and R for whole blood were obtained from non-diluted samples, and samples diluted with 1x PBS by 100 times. The purpose of diluting the blood was to enhance T for $\lambda < 604$ nm since the detector was unable to resolve the signature absorption peaks of oxyhemoglobin over the 400 – 600 nm spectral band. Since the reported range of hematocrit (hct) for bovine blood is 36.9 ± 4.2% [55], we assumed an average value of 37% hct for the blood samples used in this study for the measurements of T and R.

Blood, or NETs samples were placed on the entrance port with the exit port closed for T measurements (figure 1(a)), and on the open exit port for the R measurements (figure 1(b)). To compare T and R among different sets of NETs, in our analysis we normalized the measurements of T to the values at 740 and 806 nm for NETs formed by double extrusion and with 5 μM ICG in the loading buffer. In our analysis of R, we normalized the measurements to those at 500 nm for unextruded EGs.

Non-normalized measurements of T and R, along with an assumed values of refractive index (n) (1.33), and estimates of the anisotropy factor (g) for NETs were subsequently used as

input parameters into an Inverse Adding-Doubling (IAD) algorithm [56]. The IAD algorithm repeatedly guesses and checks solutions for the radiative transport equation until it determines values of absorption coefficient (μ_a (mm^{-1})) and reduced scattering coefficient (μ_s' (mm^{-1})) that fit the measured data T and R [56]. The μ_s' is related to the scattering coefficient (μ_s) and g (the mean cosine of the scattering function) as:

$$\mu_s' = \mu_s (1-g) \quad (1)$$

Range of g is from −1 to 1. When $g = 1$, the scattering is completely in the forward direction, and $\mu_s' = 0$. In the case of isotropic scattering ($g = 0$), and $\mu_s' = \mu_s$. For example, the reported value of g for skin is ≈ 0.5 at 400 nm, and increases to > 0.9 for wavelengths greater than 800 nm [57]. For mammalian cells, the reported g value is ≈ 0.95 in the spectral band of 425 – 900 nm [57]. Therefore, to estimate μ_s' for whole blood, we used $g = 0.95$.

For NETs, g value was estimated using a Mie Simulator (Virtual Photonics Initiative, Irvine, California) based on measurements of the NETs diameter [58]. Specifically, the g values were estimated as 0.99 for the micron-sized NET based on measurements of diameter by phase contrast imaging (figure 2(a)), 0.66 for nano-sized NETs formed by single extrusion, and 0.55 for nano-sized NETs formed by double extrusion, based on measurements of the diameter by DLS. We used these g values and the measured values of T and R in the IAD algorithm to obtain spectrally-dependent estimates of μ_s' for whole blood, EGs, micron-sized NETs formed without extrusion, and nano-sized NETs formed by single or double extrusions at ICG loading concentrations in the range of 5–20 μM.

We used a general analytical expression [57] that takes into account contributions by Rayleigh and Mie types of scattering for spherical objects to fit the estimated μ_s' spectra:

$$\mu_s'(\lambda) = A' \left[f_{\text{Rayleigh}} \left(\frac{\lambda}{\lambda_o} \right)^{-4} + \left(f_{\text{Rayleigh}} \right) \left(\frac{\lambda}{\lambda_o} \right)^{-m} \right] \quad (2)$$

where $A' = \mu_s'(\lambda_o)$, f_{Rayleigh} is the fractional contribution due to Rayleigh scattering, λ_o is a reference wavelength, and m is the power law exponent (scattering power) related to the Mie scattering component. We used $\lambda_o = 500$ nm since at this wavelength there is no absorption by NETs that may originate from either hemoglobin or ICG, and therefore, optical attenuation for NETs is completely due to scattering. Spectrally-dependent values of μ_s' within the spectral range of 437 – 635 nm were fitted by Igor Pro (Wavemetrics, Lake Oswego, Oregon) and extrapolated for $\lambda < 437$ and $\lambda < 635$ based on equation (2).

2.3. Light-distribution model

The Monte Carlo light-distribution model used in this study was developed by Majaron *et al* [59,60]. To represent μ_a and μ_s of human whole blood with 45% hct [57,61], we scaled our estimates of μ_a and μ_s associated with assumed value of 37% hct as follows:

$$\mu_{\mathrm{a}}\ (45\%\ \mathrm{hct}) = \mu_{\mathrm{a}}\ (37\%\ \mathrm{hct}) \left(\frac{0.45}{0.37}\right) \quad (3)$$

$$\mu_{\mathrm{s}}^{'}\ (45\%\ \mathrm{hct}) = \mu_{\mathrm{s}}^{'}\ (37\%\ \mathrm{hct}) \left(\frac{0.45}{0.37}\right) \quad (4)$$

We simulated 1,000,000 photons delivered to a 500 μm diameter blood vessel containing either blood at 45% hct without any added NETs, or with added nano- or micron-sized NETs (sets I–III). We note that this simulation is not representative of a skin with PWS. A PWS simulation would require additional features including a multi-layered geometry to account for the presence of epidermis and additional blood vessels. Herein, we only seek to investigate the relative optical response of a blood vessel with and without NETs. We used the scaled optical properties of blood (equations 3 and 4), and NETs obtained in this study. We assumed effective optical properties of the simulated blood vessel as:

$$\mu_{\mathrm{a\_BV}} = f_{\mathrm{blood}} \mu_{\mathrm{a\_blood}}\ (45\%\ \mathrm{hct}) + (1 - f_{\mathrm{NETs}})\ \mu_{\mathrm{a\_NETs}} \quad (5)$$

$$\mu_{\mathrm{s\_BV}}^{'} = f_{\mathrm{blood}} \mu_{\mathrm{s\_blood}}^{'}\ (45\%\ \mathrm{hct}) + (1 - f_{\mathrm{NETs}})\ \mu_{\mathrm{s\_NETs}}^{'} \quad (6)$$

where $\mu_{\mathrm{a\_BV}}$ is the effective absorption coefficient of the blood vessel, f_{blood} and f_{NETs} are the respective fractions of blood and NETs in the blood vessel (f_{blood} = f_{NETs} = 50%), $\mu_{\mathrm{a\_blood}}$ (45% hct) and $\mu_{\mathrm{a\_NETs}}$ are the respective absorption coefficients of blood with 45% hct and NETs, and $\mu_{\mathrm{s}}^{'}{}_{\mathrm{\_BV}}$ (45% hct) and $\mu_{\mathrm{s}}^{'}{}_{\mathrm{\_NETs}}$ are the effective reduced scattering coefficient of the blood vessel and NETs, respectively. We simulated a flat-top incident laser beam at 806 nm corresponding to peak absorption wavelength associated with the monomeric form of ICG in NETs. The beam delivered fluence of 10 J/cm^2, and illuminated a 100 μm diameter spot on the surface.

3. RESULTS AND DISCUSSION

3.1. Size distribution of NETs

The average ± standard deviation (SD) diameter for micron-sized NETs, formed without mechanical extrusion, was 4.31 ± 0.69 μm (n=28) (figure 2(a)). This mean value is smaller than the reported average diameter of bovine red blood cells (5.05 μm), but within the reported SD (± 0.16 μm) [62]. The hydrodynamic peak (d_{peak}) diameters, as determined by DLS technique, were ≈ 164 nm (polydispersity index (PDI) = 0.10) and 91nm (PDI = 0.07) for the populations of nano-sized respectively (figure 2(b)). We used lognormal fits to estimate the mean (d_{mean}) ± SD diameters of single extruded (160 ± 2 nm), and double

extruded (92 ± 1 nm) NETs. The population of the nano-sized NETs is considered to be mono- dispersed since the respective PDI values are equal to, or less than 0.1 [63].

Since particles with diameters < 200 nm are more effective for extravasation into tumors through the EPR effect [64], nano-sized NETs may prove as effective nano-vesicles with light-based theranostic capabilities for fluorescence imaging and photo-destruction of tumors. Further molecular specificity of NETs can be achieved by functionalizing their surface with appropriate targeting moieties such as antibodies [48].

3.2. Transmittance and reflectance measurements

The measurement results for T and R for micron-sized NETs formed without extrusion ($d_{mean} \approx 4.31$ μm), and nano-sized NETs formed by single ($d_{mean} \approx 160$ nm) or double extrusions ($d_{mean} \approx 92$ nm) using ICG loading concentrations in the range of 5–20 μM are shown in figure 3. We also present the results for whole blood, and EGs not containing ICG in these figures.

The non-diluted blood sample showed less than 3% transmission over the approximate spectral band of 400 – 610 nm (figure 3(a)), indicative of the relatively high light absorption by hemoglobin in this wavelength range. Therefore, this sample was diluted by 100 times to resolve transmission changes over this spectral band. Minimum values of T at 420, 542, and 577 nm for the diluted blood sample (figure 3(a)) are indicative of hemoglobin absorption at these wavelengths. We attribute the relatively high values of $T(\lambda > 610$ nm) for the diluted sample to reduced number of erythrocytes and the overall lower absorption by hemoglobin at these wavelengths. The nearly constant value of $T(\lambda > 610$ nm) is suggestive of the Fresnel reflection at the interface of the sample solution and the cuvette.

It is important to note that the values of T for all sets of NETs nearly overlapped with those for the EGs except over the approximate bands of 400 – 440 nm and 630 – 865 nm, indicative of successful loading of ICG into the NETs. For EGs, T spectra did not show a decreasing trend over the 630 – 865 nm spectral band, consistent with the fact that these particles did not contain ICG. For the three sets of NETs having d_{mean} values in the range of ≈ 92 nm – 4.31 μm, as the concentration of ICG in the loading buffer increased, there was an overall trend in T values becoming lower over the 630 – 865 nm spectral band (figures 3(c), (e), (g)), indicating that higher concentrations of ICG were loaded into the particles. Independent of the d_{mean} value, minimum values of T occurred between 803 and 806 nm, which corresponds to peak absorption wavelength associated with monomeric form of ICG. As a quantitative example, for NETs fabricated using ICG concentration of 20 μM in the loading buffer, T values associated with the monomer form of ICG decreased by about 4.5 times as d_{mean} of NETs was increased from ≈ 92 nm to 4.31 μm (figure 3(i)).

We attribute the shoulder in the approximate spectral range of 720 – 760 nm (albeit without a distinct secondary peak) to the H-like aggregate forms of ICGs within the [47,65]. Aggregation-induced split in the excited electronic state that results from a stacked (sandwich-like) arrangement of the individual chromophores, and their transition dipole moments constitute H-aggregation [66–68]. In H-aggregates, transitions to the upper level of the split excited state are allowed, resulting in a blue spectral shift.

With increased ICG concentration, the T value in the range of 720 – 760 nm decreased for the three sets of NETs, suggesting higher levels of ICG in the aggregated form within the NETs. For example, for NETs fabricated using ICG concentration of 5 μM in the loading buffer, T values associated with the H-like aggregate form of ICG decreased by about 10% as d_{mean} of NETs was increased from ≈ 92 nm to 4.31 μm (figures 3(c), (e), (g)). Collectively, these results indicate that more ICG can be loaded into the larger diameter NETs, and that the relative fraction of monomeric form of ICG is consistently higher than the H-like aggregate forms when using ICG in the range of 5–20 μM to fabricate these three sets of NETs.

We summarize some of the salient features of T for NETs in figure 3(i) where the measurements are normalized to the values at 740 nm and 806 nm for 92 nm NETs formed using 5 μM ICG in the loading buffer. At a given ICG concentration, as the NETs diameter became larger, normalized transmittance values (T_{norm}) becomes smaller. For both micron- and nano-sized NETs, T_{norm} values decreased with increasing ICG concentration.

For the non-diluted whole blood sample, the relatively low values of R (< 6%) in the approximate spectral range of 400 – 600 nm (figure 3(b)) are likely due to loss of photons to absorption by hemoglobin in this spectral band. For wavelengths greater than the spectral peak at 674 nm, R values decreased, suggestive of decreased light absorption by hemoglobin, and decreased scattering by erythrocytes. For the whole blood sample diluted by 100 times, the R values were less than 4% over the entire spectral band investigated (400–1000 nm), suggesting that there were relatively fewer scattering objects (e.g., erythrocytes) within the sample to make sufficient back-scattered photons available for detection as compared with the non-diluted sample.

For the three sets of NETs, with increased ICG concentration in the loading buffer, there was an overall trend in R values becoming smaller over the approximate spectral band of 600 – 795 nm (figures 3(d), (f), (h)). The peak R values were at 453 nm, 444 nm and 440 nm, corresponding to NETs with d_{mean} ≈ 4.31 μm, 160 nm and 92 nm respectively. For a given d_{mean}, the peak R values varied only by about 0.9 – 1.3% as the ICG concentration increased from 5 to 20 μM. For all ICG concentrations used in fabricating these NETs, peak R values for micron-sized NETs (d_{mean} ≈ 4.31 μm) were consistently higher by approximately 8% than those for nano-sized NETs with d_{mean} ≈ 92 nm. This result suggests that increased levels of ICG used during fabrication do not contribute much to the reflectance from the particles at the peak reflectance wavelengths (outside the ICG absorption band), and the higher R values associated with the larger NETs are likely due to the enhanced back-scattering that results from increased diameter of the particles.

In figure 3(j), we show a summary of R measurements normalized to the value at 500 nm (spectral peak) for EGs. At this wavelength, there are minimal contributions from absorption by hemoglobin and ICG, and therefore, R can be mostly contributed to back-scattering by the particles. At a given ICG concentration, normalized reflectance values (R_{norm}) became larger as NETs diameter increased. For both micron- and nano-sized NETs, R_{norm} values at 500 nm remained nearly independent of ICG concentration.

3.3. Absorption coefficient (μ_a) of NETs

We used the measured values of T and R (figure 3) in an Inverse Adding-Doubling (IAD) algorithm (Prahl *et al* 1993) to estimate the values of μ_a for micron-sized NETs formed without extrusion ($d_{mean} \approx 4.31$ μm), and nano-sized NETs formed by single ($d_{mean} \approx 160$ nm) and double extrusions ($d_{mean} \approx 92$ nm) at ICG loading concentrations in the range of 5–20 μM (figure 4). We also present the results for blood samples, and EGs not containing ICG in these figures.

The estimated μ_a spectra for whole blood were obtained by using the T and R spectra of the diluted sample in the 400 – 604 nm range, and T and R spectra associated with $\lambda > 604$ nm for the non-diluted sample in the IAD algorithm values. The estimated μ_a values over the 400 – 604 nm range were then multiplied by 100 to account for the dilution factor during T and R measurements.

The spectral peaks of μ_a at 420, 542, 581 nm (figure 4(a)) are associated with oxyhemoglobin. The respective μ_a values of 25 and 23 mm^{-1} at 542 and 581 nm are in excellent agreement with the values of 29 and 23 mm^{-1} at these wavelengths reported in a review article by Jacques [57], and available in a tabulated form [69]. Our estimated μ_a value of 59 mm^{-1} at 420 nm is lower than the reported values of 115 and 257 mm^{-1} at this wavelength [69,61]. This difference may be due to the relatively low intensity of the quartz-tungsten-halogen lamp used during the measurements of T and R, at wavelengths close to 400 nm, which could lead to a lower value of the difference between reference and measured T, and subsequent under-estimation of μ_a. These overall agreements in spectral characteristics of μ_a with those in literature confirm the validity of our R and T measurements and the associated IAD algorithm in estimating $\mu_a(\lambda)$ for blood, and subsequently, the NETs in this study.

For these sets of NETs (figures 4(b), (c), (d)), absorption peaks associated with oxyhemoglobin at 415, 542, and 577 nm, and those associated with deoxyhemoglobin at 439 and 555 nm are greatly diminished, indicating partial or complete depletion of hemoglobin during fabrication of NETs [70]. Consistent with a previous report [71], the absorption peak at 414 nm is attributed to ICG, and for the three sets of NETs, its value in general increased with increasing values of ICG concentration used during fabrication.

For the three sets of NETs, there was an overall trend of increasing μ_a values over the approximate spectra range of 630 – 860 nm as the concentration of ICG in the loading buffer increased. NETs of all diameters had maximum value of μ_a at 806 nm, and a shoulder in the range of ≈ 720 – 760 nm, which correspond to the peak absorption wavelength associated with the monomeric and H-like aggregate forms of ICG within NETs, respectively. For EGs, μ_a spectra did not show a spectral peak at 806 nm or a distinct shoulder, consistent with the fact that ICG was not present in the EGs.

We summarize the values of μ_a for NETs at wavelengths associated with monomeric (806 nm) and H-like aggregate (740 nm) forms of ICG in figure 4(e). There was a nearly linear increase in μ_a at these wavelengths with increasing ICG concentration in the range of 5–20 μM for micron- and nano-sized NETs, indicating that the ICG content within the NETs

increased regardless of the NETs diameter. For example, as ICG concentration in the loading buffer increased from 5 to 20 μM, μ_a (λ = 806 nm) increased by ≈ 4.6 times for micron-sized NETs (d_{mean} ≈ 4.31 μm), and ≈ 3.0 times for nano-sized NETs with d_{mean} ≈ 92 nm. In general, at a given ICG concentration, as the NETs diameter increased from nano-sized (d_{mean} ≈ 92 nm) to micron-sized (d_{mean} ≈ 4.31 μm), higher amounts of ICG could be loaded into the micron-sized NETs, as evidenced by higher values of μ_a at these wavelengths for the micron-sized NETs.

3.4. Reduced scattering coefficient (μ_s') of NETs

The diameters of cellular components of whole blood (e.g., erythrocytes) and these NETs (in the range of ≈ 90 nm – 4 μm) are comparable to or larger than the investigated wavelength range of 400 nm – 1000 nm. Therefore, it is expected that the scattering behavior of whole blood and NETs can be described by Mie scattering. Best fits to the estimated values of μ_s' for λ > 620 nm were obtained with $f_{Rayleigh}$ = 0, and m = 0.517 based on the T and R values for non-diluted blood sample.

Our estimated values of ≈ 2 – 1.4 mm^{-1} for μ_s' in the range of 620 – 1000 nm are consistent with the reported values of ≈ 1.5 – 1.3 mm^{-1} in this spectral range [61]. The inability to fit the μ_s' values for λ < 620 nm results from an inherent limitation of the IAD algorithm when the T and R values are relatively low. In particular, these values were less than 6% for the non-diluted blood samples for T (λ < 620 nm) and R (λ < 600 nm). These low values are interpreted by the IAD algorithm as lost photons, and not available to make a contribution towards scattering; therefore, under-estimating μ_s' as compared to theoretical values provided by the analytical expression in equation (2).

Successful fits to μ_s' profiles in the approximate spectral band of 440 – 635 nm were obtained with $f_{Rayleigh}$ = 0, and respective values of m = 1.30, 1.35, and 2.60 for NETs formed without extrusion (d_{mean} ≈ 4.31 μm) and by single extrusion (d_{mean} ≈ 160 nm) or double extrusions (d_{mean} ≈ 92 nm). We extrapolated these fits to be consistent with Mie theory. Deviations from the analytical fits for λ < 440 nm and λ > 635 nm are due to limitations of the IAD algorithm. The algorithm under-estimates the values of μ_s' when λ < 440 nm or λ > 635 nm, likely due to the decrease in R values of the NETs over these spectral bands. For the micron-sized NETs (d_{mean} ≈ 4.31 μm), and the nano-sized NETs (d_{mean} ≈ 92 nm), the IAD algorithm tends to over-estimate the μ_s' over the 828 – 863 nm spectral band, possibly due to the T values > ≈ 10% and low R values < ≈ 6% associated with these NETs at these wavelengths.

Estimated values of m increased as the diameter of the NETs decreased, and appeared to follow a trajectory to reach the scattering power of 4 (associated with Rayleigh scattering) if the NETs diameter were to become smaller. The estimated values of m in the range of 1.30 and 2.60 are similar to those reported for soft tissues such as brain (m = 1.2) [72], heart (m = 1.26) [72], prostate (m = 1.52) [73], and breast (m = 2.74) [74].

For all sets of NETs, values of μ_s' decreased with increasing wavelength in accordance with the analytical expression for Mie scattering, and were minimally dependent on ICG

concentration used in fabricating them. While values of μ_s' were similar for the nano-sized NETs, they increased for the micron-sized NETs at the corresponding wavelengths.

We summarize the estimated values of μ_s' at 500 nm, a wavelength at which there is little contributions from absorption by hemoglobin and ICG, in figure 5(e). For both micron- and nano-sized NETs, μ_s' (λ = 500 nm) remained nearly independent of ICG concentration. At all ICG concentrations, values of μ_s' (λ = 500 nm) for micron-sized NETs were ≈ 2.2 times higher than those for nano-sized NETs.

3.5 Monte carlo simulation of light distribution in blood vessels containing NETs

We used the estimated values of g by the Mie Simulator (Virtual Photonics Initiative, Irvine, California), the estimated values μ_a by the IAD algorithm, and the predicated values of μ_s' according to Mie scattering in a Monte Carlo-based model to simulate the light distribution in response to 806 nm laser irradiation of blood vessels containing NETs (figures 6(a–f)). We assumed that the optical properties of the blood vessel were based on either 45% hematocrit (hct) without NETs (figure 6(a)), or 45% hct plus 50% NETs (figures 6(b–f)), and that the incident fluence was 10 J/cm^2 with the laser beam focused onto a 100 μm diameter spot. In figure 6(g), we show the resulting fluence levels as a function of the depth along the central axis of the laser beam.

Doping the blood vessel with NETs enhanced the fluence levels (figures 6(b–g)). While increased fluence values above the incident level, due to back-scattering [75], were predicted within the blood vessel without NETs, the subsurface peak fluence values were further amplified in the presence of NETs.

Nano-sized NETs of d_{mean} ≈ 160 nm and micron-sized NETs, fabricated using 20 μM ICG, produced similar fluence levels within the depth of ≈ 100 μm; however, at depths greater than 100, higher fluence levels were predicted by the micron-sized NETs (figures 6(d), (g)). Increasing the ICG concentration from 5 μM to 20 μM resulted in an overall increase in fluence values for up to ≈ 300 μm within the blood vessel doped with NETs having d_{mean} ≈ 92 nm (figures 6(b–d, g)). Doping the blood vessel with micron-sized NETs (d_{mean} ≈ 4.31 μm) produced higher fluence values deeper into the blood vessel when compared to nano-sized NETs (figure 6(f), (g)), attributed to higher forward scattering (g = 0.99). These results imply that for light-mediated destruction of large blood vessels, micron-sized NETs may provide better efficacy in terms of offering the ability to achieve higher fluences deeper into the blood vessel.

4. Conclusions

We report, for the first time, the optical properties of NETs as a function of their diameters and the ICG concentration level used in fabricating them. Our results demonstrate that for a given NETs diameter, values of μ_a increased over the approximate spectral band of 630 – 860 nm with increasing ICG concentration. Micron-sized NETs produced the highest peak value of μ_a when using ICG concentrations of 10 and 20 μM as compared to nano-sized NETs. For these NETs, spectral profiles of μ_s' were minimally affected by ICG concentration used in fabricating the NETs. Micron-sized NETs had higher values of μ_s' as

compared to nano-sized NETs. Knowledge of the NETs optical properties establishes a framework for development of mathematical models aimed at predicting the optical response of biological tissues containing NETs. Additionally, optical properties of NETs are important in guiding the selection of appropriate light dosimetry parameters for various light-based biomedical application of NETs.

Acknowledgments

This study was supported in parts by grants from the National Institute of Arthritis and Musculoskeletal and Skin Diseases (1R01-AR068067-01A1), National Science Foundation (CBET-1509218), Laser Microbeam and Medical Program (LAMMP: P41-EB015890-33), an NIH/NIBIB Biotechnology Resource Center, University of California Cancer Research Coordinating Committee (5-441894-34812), and University of California, Riverside Office of Research & Economic Development.

References

1. Kim H, Chung K, Lee S, Kim DH, Lee H. Near-infrared light-responsive nano-materials for cancer theranostics. WIREs Nanomed Nanobiotechnol. 2016; 8:23–25.
2. Cheng L, Yuan C, Shen S, Yi X, Gong H, Yang K, Liu Z. Bottom-up synthesis of metal-ion-doped WS2 nanoflakes for cancer theranostics. ACS Nano. 2015; 9:11090–11101. [PubMed: 26445029]
3. Shan G, Weissleder R, Hilderbrand SA. Upconverting organic dye doped core-shell nano-composites for dual-modality NIR imaging and photo-thermal therapy. Theranostics. 2013; 3:267–274. [PubMed: 23606913]
4. Lee M-Y, Lee C, Jung HS, Jeon M, Kim KS, Yun SH, Kim C, Hahn SK. Biodegradable photonic melanoidin for theranostic applications. ACS Nano. 2016; 10:822–831. [PubMed: 26623481]
5. Lin L-S, Yang X, Niu G, Song J, Yang H-H, Chen X. Dual-enhanced photothermal conversion properties of reduced graphene oxide-coated gold superparticles for light-triggered acoustic and thermal theranostics. Nanoscale. 2016; 8:2116–2122. [PubMed: 26726809]
6. Win KY, Teng CP, Ye E, Low M, Han MY. Evaluation of polymeric nanoparticle formations by effective imaging and quantitation of cellular uptake for controlled delivery of doxorubicin. Small. 2015; 11:1197–1204. [PubMed: 25400129]
7. Frangioni JV. In vivo near-infrared fluorescence imaging. Curr Opin Chem Biol. 2003; 7:626–634. [PubMed: 14580568]
8. Marshall MV, Rasmussen JC, Tan I-C, Aldrich MB, Adams KE, Wang X, Fife CE, Maus EA, Smith LA, Sevick-Muraca EM. Near-infrared fluorescence imaging in humans with indocyanine green: a review and update. Open Surg Oncol J. 2010; 2:12–25. [PubMed: 22924087]
9. Hadjipanayis CG, Jiang H, Roberts DW, Yang L. Current and future clinical applications for optical imaging of cancer: from intraoperative surgical guidance to cancer screening. Semin Oncol. 2011; 38:109. [PubMed: 21362519]
10. Roessler K, Krawagna M, Dorfler A, Buchfelder M, Ganslandt O. Essentials in intraoperative indocyanine green videoangiography assessment for intracranial aneurysm surgery: conclusions from 295 consecutively clipped aneurysms and review of the literature. Neurosurg Focus. 2014; 36:E7.
11. Crane LMA, Themelis G, Arts HJG, Buddingh KT, Brouwers AH, Ntziachristos V, van Dam GM, van der Zee AGJ. Intraoperative near-infrared fluorescence imaging for sentinel lymph node detection in vulvar cancer: first clinical results. Gynecol Oncol. 2011; 120:291–295. [PubMed: 21056907]
12. Hirche C, Murawa D, Mohr Z, Kneif S, Hunerbein M. ICG fluorescence-guided sentinel node biopsy for axillary nodal staging in breast cancer. Breast Cancer Res Treat. 2010; 121:373–378. [PubMed: 20140704]
13. Ishikawa K, Yasuda K, Shiromizu A, Etoh T, Shiraishi N, Kitano S. Laparoscopic sentinel node navigation achieved by infrared ray electronic endoscopy system in patients with gastric cancer. Surg Endosc. 2007; 21:1131–1134. [PubMed: 17180275]

14. Sevick-Muraca EM, Sharma R, Rasmussen JC, Marshall MV, Wendt JA, Pham HQ, Bonefas E, Houston JP, Sampath L, Adams KE, Blanchard DK, Fisher RE, Chiang SB, Elledge R, Mawad ME. Imaging of lymph flow in breast cancer patients after microdose administration of a near-infrared fluorophore: feasibility study. Radiology. 2008; 246:734–741. [PubMed: 18223125]
15. van der Vorst JR, Schaafsma BE, Verbeek FPR, Swijnenburg RJ, Hutteman M, Liefers GJ, van de Velde CJH, Frangioni JV, Vahrmeijer AL. Dose optimization for near-infrared fluorescence sentinel lymph node mapping in patients with melanoma. Brit J Dermatol. 2013; 168:93–98. [PubMed: 23078649]
16. Verbeek FPR, Troyan SL, Mieog JSD, Liefers G-J, Moffitt LA, Rosenberg M, Hirshfield-Bartek J, Gioux S, van de Velde CJH, Vahrmeijer AL, Frangioni JV. Near-infrared fluorescence sentinel lymph node mapping in breast cancer: a multicenter experience. Breast Cancer Res Treat. 2014; 143:333–342. [PubMed: 24337507]
17. Zaidi HA, Abla AA, Nakaji P, Chowdhry SA, Albuquerque FC, Spetzler RF. Indocyanine green angiography in the surgical management of cerebral arteriovenous malformations: lessons learned in 130 consecutive cases. Neurosurgery. 2014; 10(Suppl 2):246–251. [PubMed: 24535264]
18. Liggett PE, Lavaque AJ, Chaudhry NA, Jablon EP, Quiroz-Mercado H. Preliminary results of combined simultaneous transpupillary thermotherapy and ICG-based photodynamic therapy for choroidal melanoma. Ophtalmic Surg Lasers Imaging. 2005; 36:463–470.
19. Klein A, Baumler H, Buschmann M, Landthaler M, Babilas P. A randomized controlled trial to optimize indocyanine green-augmented diode laser therapy of capillary malformations. Lasers Surg Med. 2013; 45:216–224. [PubMed: 23619901]
20. Klein A, Szeimies RM, Baumler W, Zeman F, Schreml S, Hohenleutner U, Landthaler M, Koller M, Babilas P. Indocyanine green-augmented diode laser treatment of port-wine stains: clinical and histological evidence for a new treatment option from a randomized controlled trial. Brit J Dermatol. 2012; 167:333. [PubMed: 22435991]
21. Kirchherr AK, Briel A, Mäder K. Stabilization of indocyanine green by encapsulation within micellar systems. Mol Pharm. 2009; 6:480–491. [PubMed: 19228053]
22. Rodriguez VB, Henry SM, Hoffman AS, Stayton PS, Li X, Pun SH. Encapsulation and stabilization of indocyanine green within poly(styrene-alt-maleic anhydride) block-poly(styrene) micelles for near-infrared imaging. J Biomed Opt. 2008; 13:014025. [PubMed: 18315383]
23. Wu L, Fang S, Shi S, Deng J, Liu B, Cai L. Hybrid polypeptide micelles loading indocyanine green for tumor imaging and photothermal effect study. Biomacromolecules. 2013; 14:3027. [PubMed: 23941524]
24. Kraft JC, Ho RJ. Interactions of indocyanine green and lipid in enhancing near-infrared fluorescence properties: the basis for near-infrared imaging in vivo. Biochemistry. 2014; 53:1275–1283. [PubMed: 24512123]
25. Mordon S, Desmettre T, Devoisselle JM, Soulie S. Thermal damage assessment of blood vessels in a hamster skin flap model by fluorescence measurement of a liposome-dye system. Lasers Surg Med. 1997; 20:131–141. [PubMed: 9047166]
26. Toyota T, Fujito H, Suganami A, Ouchi T, Ooishi A, Aoki A, Onoue K, Muraki Y, Madono T, Fujinami M, Tamura Y, Hayashi H. Near-infrared-fluorescence imaging of lymph nodes by using liposomally formulated indocyanine green derivatives. Bioorg Med Chem. 2014; 22:721–727. [PubMed: 24393719]
27. Bahmani B, Gupta S, Upadhyayula S, Vullev VI, Anvari B. Effect of polyethylene glycol coating on uptake of indocyanine green loaded nanocapsules by human spleen macrophages in vitro. J Biomed Opt. 2011; 16:051303. [PubMed: 21639563]
28. Saxena V, Sadoqi M, Shao J. Polymeric nanoparticulate delivery system for indocyanine green: biodistribution in healthy mice. Int J Pharm. 2006; 308:200–204. [PubMed: 16386861]
29. Yaseen MA, Yu J, Wong MS, Anvari B. Stability assessment of indocyanine green within dextran-coated mesocapsules by absorbance spectroscopy. J Biomed Opt. 2007; 12:064031. [PubMed: 18163847]
30. Zheng X, Zhou F, Wu B, Chen WR, Xing D. Enhanced tumor treatment using biofunctional indocyanine green-containing nanostructure by intra tumoral or intravenous injection. Mol Pharm. 2012; 9:514–522. [PubMed: 22332810]

31. Sharma P, Bengtsson NE, Walter GA, Sohn H-B, Zhou G, Iwakuma N, Zeng H, Grobmyer SR, Scott EW, Moudgil BM. Gadolinium-doped silica nanoparticles encapsulating indocyanine green for near infrared and magnetic resonance imaging. Small. 2012; 8:2856–2868. [PubMed: 22744832]
32. Yoo J-W, Irvine DJ, Discher DE, Mitragotri S. Bio-inspired, bioengineered and biomimetic drug delivery carriers. Nat Rev Drug Discov. 2011; 10:521–535. [PubMed: 21720407]
33. Pierigè F, Serafini S, Rossi L, Magnani M. Cell-based drug delivery. Adv Drug Deliv Rev. 2008; 60:286–295. [PubMed: 17997501]
34. Muzykantov VR. Drug delivery by red blood cells: vascular carriers designed by Mother Nature. Expert Opin Drug Deliv. 2010; 7:403–427. [PubMed: 20192900]
35. Madsen SJ, Baek S-K, Makkouk AR, Krasieva T, Hirschberg H. Cell-based delivery systems for nanoshells in photothermal therapy. Ann Biomed Eng. 2012; 40:507–515. [PubMed: 21979168]
36. Kwon YM, Chung HS, Moon C, Yockman J, Park YJ, Gitlin SD, David AE, Yang VC. L-Asparaginase encapsulated intact erythrocytes for treatment of acute lymphoblastic leukemia (ALL). J Control Release. 2009; 139:182–189. [PubMed: 19577600]
37. Antonelli A, Magnani M. Red blood cells as carriers of iron oxide-based contrast agents for diagnostic applications. J Biomed Nanotechnol. 2014; 10:1732–1750. [PubMed: 25992439]
38. Oldenborg PA. CD47: a cell surface glycoprotein which regulates multiple functions. ISRN Hematol. 2013; 2013:614619. [PubMed: 23401787]
39. Rodriguez PL, Harada T, Christian DA, Pantano DA, Tsai RK, Discher DE. Minimal 'self' peptides that inhibit phagocytic clearance and enhance delivery of nanoparticles. Science. 2013; 339:971–975. [PubMed: 23430657]
40. Brähler M, Georgieva R, Buske N, Müller A, Müller S, Pinkernelle J, Teichgräber U, Voigt A, Bäumler H. Magnetite-loaded carrier erythrocytes as contrast agents for magnetic resonance imaging. Nano Lett. 2006; 6:2505–2509. [PubMed: 17090081]
41. Antonelli A, Sfara C, Manuali E, Bruce IJ, Magnani M. Encapsulation of superparamagnetic nanoparticles into red blood cells as new carriers of MRI contrast agents. Nanomedicine (Lond). 2011; 6:211223.
42. Chang M, Hsiao J-K, Yao M, Chien L-Y, Hsu S-C, Ko B-S, Chen S-T, Liu H-M, Chen Y-C, Yang C-S, Huang D-M. Homologous RBC-derived vesicles as ultrasmall carriers of iron oxide for magnetic resonance imaging of stem cells. Nanotechnology. 2010; 21:235103. [PubMed: 20479509]
43. Ahn S, Jung SY, Seo E, Lee SJ. Gold nanoparticle-incorporated human blood cells (RBCs) for X-ray dynamic imaging. Biomaterials. 2011; 32:7191–7199. [PubMed: 21777977]
44. Flower R, Peiretti E, Magnani M, Rossi L, Serafini S, Gryczynski Z, Gryczynski I. Observation of erythrocyte dynamics in the retinal capillaries and choriocapillaris using ICG-loaded erythrocyte ghost cells. Invest Ophthalmol Vis Sci. 2008; 49:5510–5516. [PubMed: 18708621]
45. Milanick MA, Ritter S, Meissner K. Engineering erythrocytes to be erythrosensors: first steps. Blood Cells Mol Dis. 2011; 47:100–106. [PubMed: 21641241]
46. Ritter SC, Milanick MA, Meissner KE. Encapsulation of FITC to monitor extracellular pH: a step towards the development of red blood cells as circulating blood analyte biosensors. Biomed Opt Express. 2011; 2:2012–2021. [PubMed: 21750776]
47. Bahmani B, Bacon D, Anvari B. Erythrocyte-derived photo-theranostic agents: hybrid nano-vesicles containing indocyanine green for near infrared imaging and therapeutic applications. Sci Rep. 2013; 3:2180. [PubMed: 23846447]
48. Mac JT, Nuñez V, Burns JM, Guerrero YA, Vullev VI, Anvari B. Erythrocyte-derived nano-probes functionalized with antibodies for targeted near infrared fluorescence imaging of cancer cells. Biomed Opt Express. 2016; 7:1311. [PubMed: 27446657]
49. Hu JC-M, Zhang L, Aryal S, Cheung C, Fang RH, Zhang L. Erythrocyte membrane-camouflaged polymeric nanoparticles a biomimetic delivery platform. PNAS. 2011; 108:10980–10985. [PubMed: 21690347]
50. Nakamura H, Jun F, Maeda H. Development of next-generation macromolecular drugs based on the EPR effect: challenges and pitfalls. Expert Opin Drug Deliv. 2015; 12:53–64. [PubMed: 25425260]

51. Torchilin V. Tumor delivery of macromolecular drugs based on the EPR effect. Adv Drug Deliv Rev. 2011; 63:131–135. [PubMed: 20304019]
52. Matsumura Y, Maeda H. A new concept for macromolecular therapeutics in cancer chemotherapy: mechanism of tumoritropic accumulation of proteins and the antitumor agents Smancs. Cancer Res. 1986; 46:6387–6392. [PubMed: 2946403]
53. Clerc SG, Thompson TE. A possible mechanism for vesicle formation by extrusion. Biophysical Journal. 1994; 67:475–476. [PubMed: 7919020]
54. Hunter DG, Frisken BJ. Effect of extrusion pressure and lipid properties on the size and polydispersity of lipid vesicles. Biophysical Journal. 1998; 74:2996–3002. [PubMed: 9635753]
55. Lepherd EE. Observations of equine and bovine haematocrit determinations. Aust Vet J. 1965; 41:380–384. [PubMed: 5858847]
56. Prahl SA, Van Germert MJC, Welch AJ. Determining the optical properties of turbid media by using the adding-doubling method. Appl Opt. 1993; 32:559–568. [PubMed: 20802725]
57. Jacques SL. Optical properties of biological tissues: a review. Phys Med Biol. 2013; 58:R37–R61. [PubMed: 23666068]
58. Laser Microbeam and Medical Program (LAMMP) Virtual Photonics Technology Initiative. http://www.virtualphotonics.org/
59. Majaron B, Milanič M, Premru J. Monte Carlo simulation of radiation transport in human skin with rigorous treatment of curved tissue boundaries. J Biomed Opt. 2015; 20:015002. [PubMed: 25604544]
60. Milanič M, Majaron B. Three dimensional Monte Carlo model of pulsed-laser treatment of cutaneous vascular lesions. J Biomed Opt. 2011; 16:128002. [PubMed: 22191938]
61. Bosschaart N, Edelman GJ, Aalders MCG, van Leeuwen TG, Faber DJ. A literature review and novel theoretical approach on the optical properties of whole blood. Lasers Med Sci. 2014; 29:453–479. [PubMed: 24122065]
62. Adili N, Melizi M. Preliminary study of the influence of red blood cells morphometry on the species determinism of domestic animals. Vet World. 2014; 7:219–223.
63. Nobbmann U, Morfesis A. Light scattering and nanoparticles. Mater Today. 2009; 12:52–54.
64. Peer D, Karp JM, Hong S, Farokhzad OC, Margalit R, Langer R. Nanocarriers as an emerging platform for cancer therapy. Nat Nanotechnol. 2007; 2:751–760. [PubMed: 18654426]
65. Jung B, Vullev VI, Anvari B. Revisiting indocyanine green: effects of serum and physiological temperature on absorption and fluorescence characteristics. IEEE J Sel Top Quantum Electron. 2014; 20:149–157.
66. Valdes-Aguiler O, Neckers DC. Aggregation phenomena in xanthene dyes. Accounts Chem Res. 1989; 22:171–177.
67. Herz AH. Aggregation of sensitizing dyes in solution and their adsorption onto silver halides. Adv Colloid Interfac. 1977; 8:237–298.
68. Ogawa M, Kosaka N, Choyke PL, Kobayashi H. H-type dimer formation of fluorophores: A mechanism for activatable, in vivo optical molecular imaging. ACS Chem Biol. 2009; 4:535–546. [PubMed: 19480464]
69. Prahl, S. Optical absorption of hemoglobin. 1999. http://omlc.org/spectra/hemoglobin/
70. Zonios G, Bykowski J, Kollias N. Skin melanin, hemoglobin, and light scattering properties can be quantitatively assessed in vivo using diffuse reflectance spectroscopy. J Invest Dermatol. 2001; 117:1452. [PubMed: 11886508]
71. Prahl, S. Optical Absorption of Indocyanine Green (ICG). 1998. http://omlc.org/spectra/icg/
72. Yi J, Backman V. Imaging a full set of optical scattering properties of biological tissue by inverse spectroscopic optical coherence tomography. Opt Lett. 2012; 37:4443–4445. [PubMed: 23114323]
73. Newman C, Jacques SL. Laser penetration into prostate for various wavelengths. Lasers Surg Med Suppl. 1991; 3:75–76.
74. Sandell JL, Zhu TC. A review of in-vivo optical properties of human tissues and its impact on PDT. J Biophotonics. 2011; 4:773–787. [PubMed: 22167862]

75. Anderson RR, Beck H, Bruggemann U, Farinelli W, Jacques SL, Parrish JA. Pulsed photothermal radiometry in turbid media: internal reflection of backscattered radiation strongly influences optical dosimetry. Appl Opt. 1989; 28:2256–2262. [PubMed: 20555508]

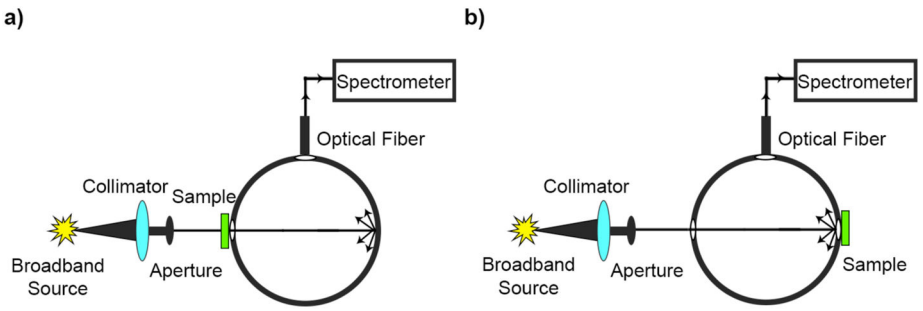

Figure 1.

Schematic of integrating sphere-based measurements of (a) transmittance and (b) reflectance for whole blood, EGs, and NET samples.

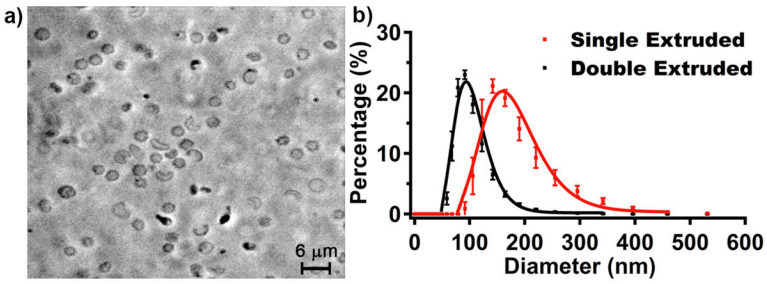

Figure 2.

Phase contrast image of micron-sized NETs (a) formed without extrusion, and hydrodynamic diameter distributions of nano-sized NETs (b) formed by single or double extrusions, as determined by DLS method. The respective ranges of the measured diameters, based on DLS, for NETs fabricated by single and double extrusion methods were ≈ 91–396 nm, and 59–190 nm. We present the mean and standard deviation of the measurements of these samples (n = 6), represented as circles and error bars, respectively. The estimated mean diameters as determined from the lognormal fits (solid curves) were ≈ 160 nm and 92 nm for NETs formed by single and double extrusion methods, respectively.

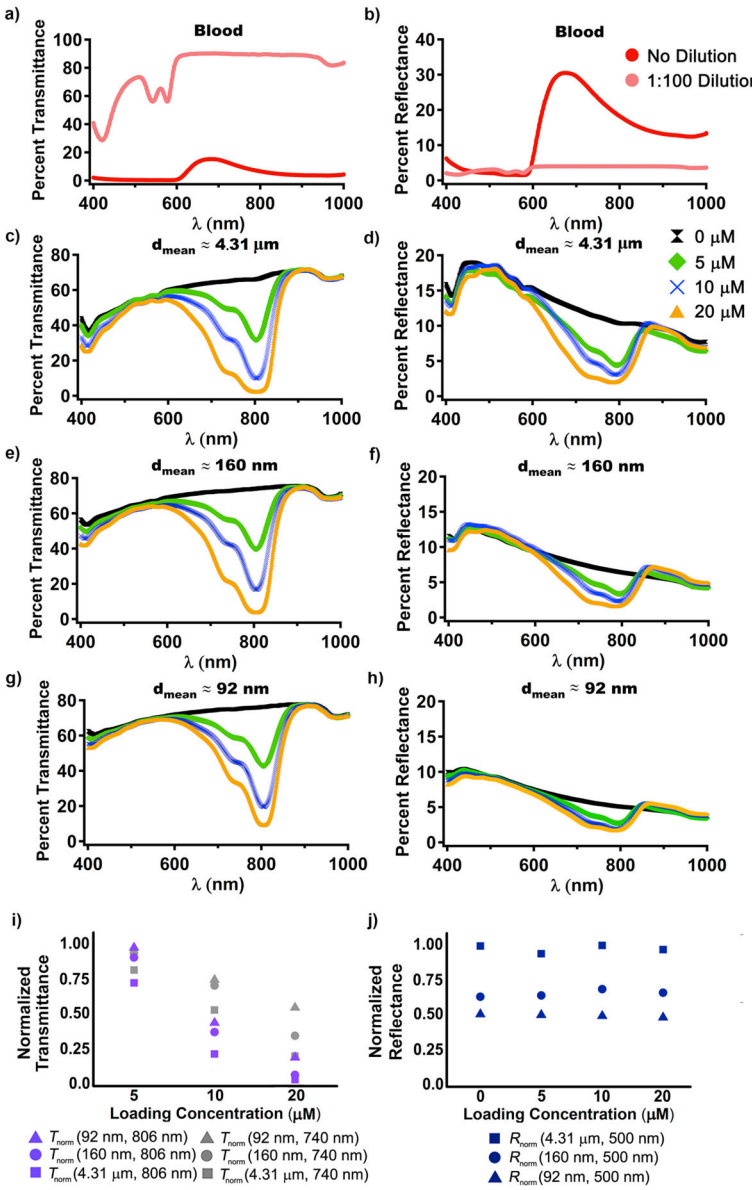

Figure 3.

Spectrally dependent values of percent transmittance (a), and reflectance (b) for whole bovine blood samples without dilution, and diluted 100 times by adding 1x PBS (≈310 mOsm). Spectra of percent transmittance (c, e, g), and reflectance (d, f, h) for micron-sized NETs formed without extrusion (c, d), or by single (e, f) or double extrusions (g, h) using various ICG concentrations. Measurements were obtained with NETs suspended in 1x PBS (≈ 310 mOsm). The legend labels indicate the ICG concentration levels in the loading buffer. In panel (i), transmittance measurements are normalized to the values at 740 nm and 806 nm for 92 nm NETs formed using 5 μM ICG in the loading buffer. In panel (j), reflectance measurements are normalized to the value at 500 nm (spectral peak) for EGs.

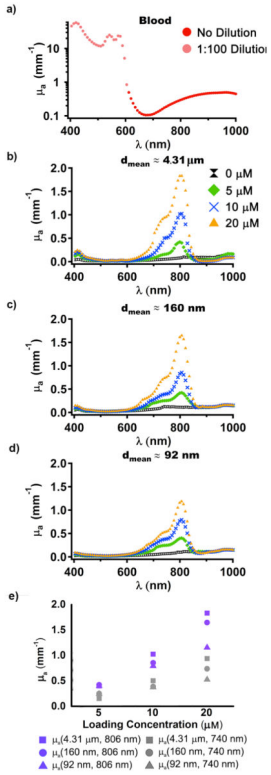

Figure 4.

Spectrally-dependent values of μ_a for whole bovine blood (a) without dilution for $\lambda > 604$ nm, and the sample diluted 100 times by adding 1x PBS (≈ 310 mOsm) for $\lambda \leq 604$ nm. Values of μ_a for the diluted sample were multiplied by 100. Spectra of μ_a for micron-sized NETs formed without extrusion (b), or by single (c) or double extrusions (d) using various ICG concentrations in the loading buffer. Measurements were obtained with NETs suspended in 1x PBS (≈ 310 mOsm). In panel (e), we show a summary of μ_a values at 740 nm and 810 nm.

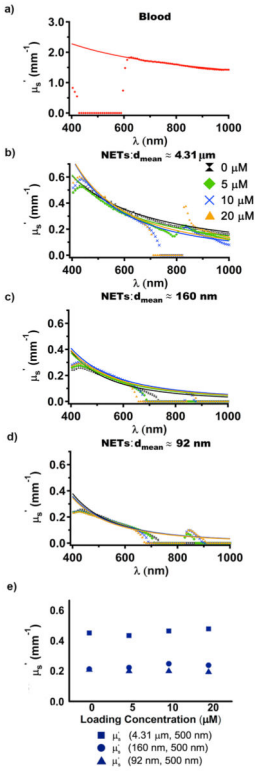

Figure 5.

Spectrally dependent values of μ_s' for whole bovine blood (a) without dilution and the fitted profile based on equation (2). Spectra of μ_s' for micron-sized NETs formed without extrusion (b), or by single (c) or double extrusions (d) using various ICG concentrations in the loading buffer, and the fitted profile based on equation (2). Measurements were obtained with NETs suspended in 1x PBS (≈ 310 mOsm). In panel (e), we show a summary of μ_s' values at 500 nm.

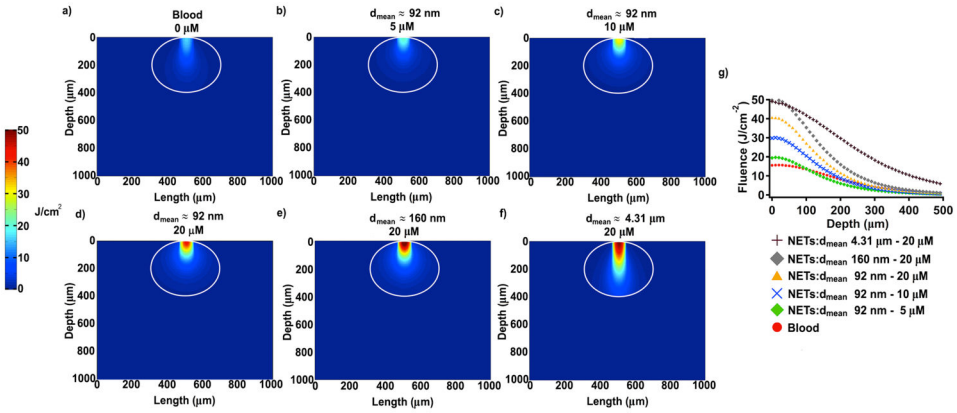

Figure 6.

Monte Carlo-based estimations of fluence profiles within a simulated 500 μm diameter blood vessel filled with blood containing 45% hematocrit without added NETs (a), or with added nano-sized NETs (d_{mean} ≈ 92 nm) (b–d), d_{mean} ≈ 160 nm NETs (c), micron-sized NETS (d_{mean} ≈ 4.31 μm). Relative fractions of blood and NETs in panels (b–e) were 50%. We utilized the optical properties of NETs formed using ICG concentrations of 5, 10, and 20 μM (b–d), and 20 μM (e, f) in the loading buffer. We assumed 806 nm laser focused on a 100 μm diameter spot at incident fluence of 10 J/cm^2. Color scale bar represents the resulting fluence in J/cm^2 and white circle represents outline of the blood vessel. The white margins delineate the boundaries of the blood vessels. In panel (g), we show the depth profile of the fluences along the central axis of the laser beam.